

AIAA '89

AIAA-89-0121

**A PATCHED-GRID ALGORITHM FOR
COMPLEX CONFIGURATIONS DIRECTED
TOWARDS THE F/A-18 AIRCRAFT**

James L. Thomas,
NASA Langley Research Center, Hampton, VA
Robert W. Walters and Taekyu Reu,
Virginia Polytechnic Institute and
State University, Blacksburg, VA
Farhad Ghaffari,
Vigyan Research Associates, Hampton, VA
Robert P. Weston and James M. Luckring,
NASA Langley Research Center, Hampton, VA

27th Aerospace Sciences Meeting

January 9-12, 1989/Reno, Nevada

A Patched-Grid Algorithm for Complex Configurations Directed Towards the F-18 Aircraft

James L. Thomas[†]

NASA Langley Research Center, Hampton, Virginia

Robert W. Walters[†]

Taekyu Reu[§]

Virginia Polytechnic Institute and State University, Blacksburg, Virginia

Farhad Ghaffari[#]

Vigyan Research Associates, Hampton, Virginia

Robert P. Weston^{*}

James M. Luckring^{*}

NASA Langley Research Center, Hampton, Virginia

Abstract

A patched-grid algorithm for the analysis of complex configurations with an implicit, upwind-biased Navier-Stokes solver is presented. Results from both a spatial-flux and a time-flux conservation approach to patching across zonal boundaries are presented. A generalized coordinate transformation with a biquadratic geometric element is used at the zonal interface in order to treat highly stretched viscous grids and arbitrarily-shaped zonal boundaries. Applications are made to the F-18 forebody-strake configuration at subsonic, high-alpha conditions. Computed surface flow patterns compare well with ground-based and flight-test results; the large effect of Reynolds number on the forebody flow-field is shown.

Nomenclature

\bar{a}_{1-6}	coefficients in surface definition
\bar{c}	mean aerodynamic chord
F, G, H	flux vectors (convective and pressure terms)
H_v	flux vector (viscous terms)
M_∞	freestream Mach number
Q	time flux vector
\vec{r}	position vector
R_o	Reynolds number based on \bar{c}
t	time
x, y, z	Cartesian coordinate system
y^+	turbulent inner-law variable
α	angle of attack, deg
ξ, η, ζ	body-fitted coordinates

[†]Senior Research Scientist, Associate Fellow AIAA

[‡]Assistant Professor, Member AIAA

[§]Research Assistant

[#]Research Engineer, Senior member AIAA

^{*}Research Engineer, Member AIAA

Introduction

There is an increasing effort in the development and application of Euler/Navier-Stokes computational algorithms for realistic aircraft configurations. Use of these prediction tools, in combination with ground-based and flight experiments, can significantly reduce the required time and cost of the design cycle. In the case of the recently proposed National AeroSpace Plane, a greater reliance must be placed on computational methods since many of the high enthalpy and high Mach number conditions are impossible to simulate with present ground-based facilities. Timeliness is a critical issue in the design cycle and there is a pressing need to reduce the overall time required for an analysis of candidate configurations which might arise in a typical design cycle.

The solvers in use today can be loosely classified into three types according to the underlying grid topology: (1) Cartesian (2) unstructured and (3) multiblock structured. The Cartesian grid solvers lead to the simplest algorithms with the fewest operations and smallest memory requirements per grid point, but are least efficient and accurate in applications to curved surfaces. With the latter two approaches, the use of body-conforming meshes leads to straightforward treatment and accurate resolution of general surfaces. The unstructured mesh solvers are the most general algorithms and their principal advantage is that grids over complex geometries can be generated in the shortest time period. However, these algorithms are also the most costly in terms of operations per time step and memory per grid point because of non-sequential memory access and the explicit connections required between the cells of the mesh.

The multiblock structured meshes are more efficient in terms of operation count and memory than the unstructured meshes, since general connection informa-

tion is restricted to the edges of the blocks. However, more constraints are placed on the grid generation process in each block, although there is an active body of ongoing research to reduce or eliminate many of these constraints. The structured mesh approach leads to the most efficient algorithms for treating viscous flows, as the grids can be highly stretched in the direction normal to the developing shear layers. Of course, the algorithm of the future is likely to be a hybrid one, with overlapping structured meshes near the body linked to a Cartesian grid in the far field through an unstructured mesh, for instance.

The present work is directed toward the development of improved techniques associated with the block structured approach, and in particular the patched grid approach. In this method, also referred to as a domain decomposition method, the computational domain is divided into a number of zones or blocks, each of which models the local geometric features and requisite physics of the configuration.¹⁻⁸ The grids in each zone can be determined independently, with the net result that the grid generation task is simpler and the solution is more efficient, since local clustering of the grid cells to resolve geometric and physical features in one region need not propagate to other blocks. The utility of the approach in a longitudinally-patched grid framework for an F-18 and an SR-71 configuration at supersonic speeds has been demonstrated previously.^{2,3} The method is extended in the present work so that the patching plane can be a general three-dimensional surface. The extension also overcomes a problem encountered in the application to viscous flows, in which a highly stretched grid is present on either side of a zonal interface.

Two approaches are described for maintaining the accuracy of the solution across the zonal interface. Applications using the two patching algorithms are made to the F-18 aircraft, at subsonic high-alpha conditions, as part of an ongoing high angle-of-attack research program being conducted by NASA. Computed surface flow patterns from solutions to the Navier-Stokes equations at $\alpha = 30$ deg are compared to ground-based experiments conducted at NASA Langley and to in-flight experiments conducted at NASA Ames-Dryden using the High Alpha Research Vehicle (HARV).⁹ The results are used to better understand the low Reynolds number ground-based tests, which are laminar and transitional, and their relationship to the flight results. A more comprehensive comparison at $\alpha = 20$ deg, including surface pressure comparisons, is given by Ghaffari et. al.¹⁰

Single Zone Algorithm

The governing equations are the time-dependent Reynolds-averaged compressible Navier-Stokes equa-

tions, cast in conservation law form and generalized coordinates as

$$\frac{\partial \hat{Q}}{\partial t} + \frac{\partial \hat{F}}{\partial \xi} + \frac{\partial \hat{G}}{\partial \eta} + \frac{\partial (\hat{H} - \hat{H}_v)}{\partial \zeta} = 0, \quad (1)$$

expressing the conservation of mass, momentum, and energy. The superscript $\hat{}$ denotes a quantity in generalized coordinates. The thin-layer form of the equations is used, where ζ is the coordinate normal to the body surface. An ideal gas is assumed; the effect of turbulence is accounted for through the concepts of an eddy viscosity and eddy conductivity. The algebraic turbulence model of Baldwin and Lomax¹¹ is used to evaluate the turbulence quantities including the modifications introduced by Degani-Schiff¹² to ensure the proper length scales are used in separated vortical flows.

The equations, while written in generalized coordinates, are solved with a semi-discrete finite-volume algorithm, resulting in a consistent approximation to the conservation laws in integral form.^{10,13,14} The convective and pressure terms are differenced with the upwind flux-difference-splitting technique of Roe.¹⁵ A MUSCL (Monotone Upstream-centered System of Conservation Laws) approach of Van Leer¹⁶ is used to determine state-variable interpolations at the cell interfaces. Each flux computation requires a single point on each side of the interface for first-order spatial differencing and two points on either side of the interface for the third-order upwind-biased spatial differencing used here. The shear stress and heat transfer terms are differenced centrally.

The equations are advanced in time to the steady state in delta form, so that the steady state is independent of the time step. Two implicit algorithms are used: (1) a spatially-factored diagonalized algorithm¹³ or (2) a hybrid algorithm, using streamwise relaxation and approximate factorization in the cross-flow planes.²

Patching Algorithm

General Concepts

The two general approaches considered for patching across zonal grids with coincident boundaries can be addressed based on the sketch in Fig. 1. Two-dimensional Cartesian grids in two zones are shown; the two zones have uniform spacing in the x -direction and a grid mismatch in the y -direction. The indices (i, j) refer to the cell-center locations of zone 1 and (l, m) to those of zone 2. The zonal interface across which the solution must be patched corresponds to the points defined as $\{x_{i+1/2, j}; j = 1, j_{max}\}$ and $\{x_{l-1/2, m}; m = 1, m_{max}\}$.

Defining the spatial flux in the x -direction as F , Rai¹ has demonstrated that global conservation can be maintained by enforcing spatial-flux conservation along the interface, as

$$\int F^{(1)}(x_{i+1/2})dy = \int F^{(2)}(x_{i-1/2})dy. \quad (2)$$

The flux in zone 2, say, is constructed from the flux in zone 1 so that Eq. (2) is satisfied. For a scheme requiring two points on either side of the interface to compute the flux, the flux in zone 1 can be constructed from the data in zone 1 and an interpolation of zone 2 data at a projection of zone 1 into zone 2. Referring to the conserved variables Q as the time flux of mass, momentum, and energy, much as F is referred to as the spatial flux of mass, momentum, and energy, the conservation of time flux in the region defined by the projected cells of zone 1 can be expressed as

$$\int \int Q^{(1)} dx dy = \int \int Q^{(2)} dx dy. \quad (3)$$

It is assumed that the grid spacing normal to the interface boundary is nominally the same between the zones to be patched. If the spacing is not the same, the error introduced is equivalent to that introduced into a single grid by a step discontinuity in the spacing. This approximation reduces the dimension of the interpolation implied by Eq. (3) by one, to a form very much like Eq. (2). For equal spacing in the x -direction, Eq. (3) becomes

$$\int Q^{(1)}(x_{i+1})dy = \int Q^{(2)}(x_i)dy. \quad (4)$$

On the other hand, the flux in zone 1 could have been constructed from zone 2 through Eq. (2), in which case a projection of zone 2 cells into zone 1 is required. The time-flux constraint equation counterpart of Eq. (4) is then

$$\int Q^{(2)}(x_{i-1})dy = \int Q^{(1)}(x_i)dy. \quad (5)$$

Ideally, all of the Eqs. (2,4,5) would be satisfied. However, any two of the three equations are sufficient to pass information between the zones. The approach which enforces Eq. (2) and either of Eqs. (4) or (5), as in the work of Rai^{1,5} and Walters et. al.^{2,3,8} is referred to as the spatial-flux conservation approach. The approach which enforces Eqs. (4) and (5) is referred to as the time-flux conservation approach. This latter approach satisfies Eq. (2) only to within truncation error but has been found, in practice, to maintain the conservative, i.e. shock-capturing, properties of the single-zone scheme as well as the former approach.^{7,8} The latter approach arises naturally in rezoning techniques for Lagrangian or adaptive mesh simulations as well as in transferring information between grids in a multigrid

calculation. For higher order spatial differencing, the above equations need to be augmented with relations representing the additional information required at the interface. For a four-point stencil at the interface, such as used in the present work, a minimum of four interpolations need to be done at an interface using either the spatial-flux or the time-flux approach.

Viewing Eq. (2) as a conservative interpolation of the time fluxes at a projection of one zone into another, it is clear that the approach does not rely on the boundaries being coincident; hence, overlapped grids, such as that used in the Chimera scheme of Benek et. al,⁴ can be accommodated. Also, the time-flux approach eliminates the departure from freestream conditions that can occur near curved interfaces using the spatial-flux approach, because of the differences in the discrete boundary definitions of the two zones.⁸

The conservative interpolations implied above can be evaluated discretely in a variety of ways. Defining the discrete flux in zone 1 to be interpolated at a particular x -position as $C_j^{(1)}$ from the discrete flux in zone 2, $C_m^{(2)}$, Rai¹ has used a piecewise-constant projection of C from one grid onto the other, as

$$C_j^{(1)} = \sum_m C_m^{(2)} N_j^m, \quad (6)$$

$$N_j^m = \begin{cases} 0, & \text{if } y_{m+1/2} < y_{j-1/2} \\ 0, & \text{if } y_{m-1/2} > y_{j+1/2} \\ \frac{1}{\Delta y_j} \int_{\max(y_{m-1/2}, y_{j-1/2})}^{\min(y_{m+1/2}, y_{j+1/2})} dy, & \text{otherwise.} \end{cases} \quad (7)$$

N_j^m represents the relative area of overlap of cell m onto the cell j , $0 \leq N_j^m \leq 1$, and the discrete flux balance is maintained, as

$$\sum_j C_j^{(1)} \Delta y_j = \sum_m C_m^{(2)} \Delta y_m,$$

since $\sum_j N_j^m \Delta y_j = \Delta y_m = y_{m+1/2} - y_{m-1/2}$. The piecewise-constant approximation is, in general, only first order accurate. Interpolating onto a coarse grid from a fine grid, the coarse grid values represent an accurate integrated average of the fine grid solution. However, interpolating onto a fine grid from a coarse grid leads to the least accurate situation, since the discrete fine grid solution reflects the "stairstep" approximation of the coarse grid. This effect can be seen in the patched-grid inlet study of Ref. 7, where an oblique shock passes from a coarse grid into a much finer one. The virtue of the approximation is its simplicity and efficiency, especially in three-dimensional applications.

For second order accuracy, the distribution of flux in zone 2 can be taken as piecewise linear,

$$C^{(2)}(y) = C_m^{(2)} + (D_y C^{(2)})_m (y - y_m),$$

for $y_{m-1/2} \leq y \leq y_{m+1/2}$, (8)

where the slope in each zone can be determined to maintain monotonicity between the zones,¹⁶ as for example,

$$(D_y C^{(2)})_m = \frac{C_{m+1}^{(2)} - C_{m-1}^{(2)}}{y_{m+1} - y_{m-1}} \phi(r_m), \quad (9)$$

$$\phi(r_m) = \frac{2r_m}{r_m^2 + 1}, \quad (10)$$

$$r_m = \frac{C_{m+1}^{(2)} - C_m^{(2)}}{C_m^{(2)} - C_{m-1}^{(2)}}. \quad (11)$$

The projection of the zone 1 grid onto the zone 2 grid gives

$$C_j^{(1)} = \sum_m [C_m^{(2)} N_j^m + (D_y C^{(2)})_m M_j^m], \quad (12)$$

$$M_j^m = \begin{cases} 0, & \text{if } y_{m+1/2} < y_{j-1/2} \\ 0, & \text{if } y_{m-1/2} > y_{j+1/2} \\ \frac{1}{\Delta y_j} \int_{\max(y_{m-1/2}, y_{j-1/2})}^{\min(y_{m+1/2}, y_{j+1/2})} (y - y_m) dy, & \text{otherwise,} \end{cases} \quad (13)$$

where the discrete flux balance is again maintained since $\sum_j M_j^m \Delta y_j = 0$. This approximation repairs the inaccuracy of the piecewise constant integration when interpolating to finer grids from coarser grids.

An alternate method within either approach is to use a nonconservative pointwise interpolation to evaluate the flux as from Eq. (8) evaluated at the cell centers of zone 2,

$$C_j^{(1)} = C^{(2)}(y_j) = C_m^{(2)} + (D_y C^{(2)})_m (y_j - y_m),$$

for $y_{m-1/2} \leq y_j \leq y_{m+1/2}$, (14)

The discrete conservation constraint equations are then satisfied only to within truncation error. The lack of complete conservation is most apparent when interpolating to a coarser mesh from a finer mesh, where the flux interpolated at the center of the coarse grid zone may not be representative of an integrated variation

of the finer grid flux over the coarser grid zone. This limitation can be removed by defining

$$C_j^{(1)} = \frac{1}{N} \sum_{p=1}^N C^{(1)}(y_p), \quad (15)$$

where $C^{(1)}(y_p)$ is defined pointwise from Eq. (8) evaluated at

$$y_p = y_{j-1/2} + \frac{2p-1}{2N} \Delta y_j, \quad p = 1, N, \quad (16)$$

representing the cell centers resulting from a division of the coarse cell zone into N smaller zones. This correction need only be used when interpolating from fine cells onto coarse cells, so that N can be chosen automatically as, for example,

$$N = \max(1, \frac{y_{j+1/2} - y_{j-1/2}}{y_{m+1/2} - y_{m-1/2}}). \quad (17)$$

In the limit of $N \rightarrow \infty$, the procedure satisfies the conservative property exactly. Exact satisfaction of the conservation equations is important for capturing weak solutions to the governing equations, such as shocks and slip surfaces. In smooth regions of the flowfield, Eq. (14) is sufficient.

Surface Patching

The counterpart in three dimensions of patching the zonal solutions along a line in two dimensions (Fig. 1) corresponds to patching along a surface. Given the three-dimensional coordinate transformation implied in Eq. (1) for each zone,

$$\vec{r} = \vec{r}(\xi, \eta, \zeta) \quad (18)$$

a patching surface can be defined without loss of generality as a surface of constant ξ . The patching algorithm must match the solution between the zones given the set of surface points on each grid defining the patching surface, as illustrated in Fig. 2 for a planar interface.

To interpolate across the interface, the transformation defined by the discrete ordered set of points in zone 1,

$$\{\vec{r}(\xi_i, \eta_j, \zeta_k) : i = 1, i_{max}; j = 1, j_{max}; k = 1, k_{max}\},$$

is used to construct at the patch interface $\xi = \text{constant}$ the generalized coordinates for the set of points in zone 2 corresponding to the patch boundary,

$$\{\vec{r}(\eta_m, \zeta_n; \xi) : m = 1, m_{max}; n = 1, n_{max}\}.$$

The equation to conserve the spatial flux at the interface $\xi = \text{constant}$ is

$$\iint \hat{F}^{(2)} d\eta d\zeta = \iint \hat{F}^{(1)} d\eta d\zeta, \quad (19)$$

which is analogous to Eq. (2) for the two-dimensional case. Likewise, the counterpart to Eq. (3) is

$$\iiint \hat{Q}^{(2)} d\xi d\eta d\zeta = \iiint \hat{Q}^{(1)} d\xi d\eta d\zeta, \quad (20)$$

where the limits of integration span the cells adjacent to the interface. The spatial-flux conservation approach uses Eqs. (19-20) to patch across the boundary; the time-flux conservation approach uses Eq. (20) and an analogous equation for the projection of zone 1 into zone 2. For higher order differencing, Eq. (20) is augmented by a similar equation relating the conserved variables in the region spanned by the second set of cells in the ξ direction adjacent to the interface. The assumption of equal spacing across the interface reduces Eq. (20) to a two-dimensional equation.

Eqs. (19-20) express the conservation relations for the redistribution of flux on one side of the interface onto the cell faces of the grid opposite the interface. Assuming a piecewise constant variation of the flux, the interpolation reduces to determining the area of overlap $N_{j,k}^{m,n}$ from the cells (m, n) of one zone onto the cells (j, k) of the other, i.e.

$$C_{j,k}^{(1)} = \sum_m \sum_n C_{m,n}^{(2)} N_{j,k}^{m,n}. \quad (21)$$

One approach to determining the area of overlap is a clipping algorithm, adapted from computer graphics, which has been used in the three-dimensional zonal calculations of Refs. 2,3, and 5. A more efficient procedure, originally developed for Lagrangian hydrodynamic rezoning calculations by Ramshaw,¹⁷ relies on the divergence theorem applied to the position vector to calculate the area as a summation of line integrals over the bounding polygons. For a linear mapping of the surface,

$$\vec{r} = \vec{a}_1 + \vec{a}_2\eta + \vec{a}_3\zeta, \quad (22)$$

the area of a cell A_p bounded by s directed line segments running from (η_1, ζ_1) to (η_2, ζ_2) is

$$A_p = \frac{|\vec{a}_2 \times \vec{a}_3|}{2} \sum_s e_s^p (\eta_1 \zeta_2 - \eta_2 \zeta_1), \quad (23)$$

where e_s^p is either +1 or -1 as the cell p lies to the left or right, respectively, of the line segment s . The areas of overlap can be calculated by sweeping over the

line segments of the two meshes, since all of the areas of overlap are formed by the intersection of mesh lines from the two surfaces. This procedure has been used in the three-dimensional calculations of Kathong et. al,⁶ Walters et. al,³ and Ghaffari et. al.¹⁰ The computational work for the area of overlap scales linearly with the number of mesh points. In a straightforward application, this procedure is more efficient than the clipping approach.³

The procedure used in most of the calculations reported here is to interpolate to the cell centers of one grid assuming a linear variation of the flux within the cells of the other grid, as

$$C_{j,k}^{(1)} = C_{m,n}^{(2)} + (D_\eta C^{(2)})_{m,n} (\eta_j - \eta_m) + (D_\zeta C^{(2)})_{m,n} (\zeta_k - \zeta_n), \quad (24)$$

for $\eta_{m-1/2} \leq \eta_j \leq \eta_{m+1/2}$, $\zeta_{n-1/2} \leq \zeta_k \leq \zeta_{n+1/2}$,

analogously to Eq. (14) in the two dimensional case. For both approaches, the geometric information describing the interpolation from one zone to another is calculated initially and then re-used at each subsequent iteration, so that the additional overhead due to the patching is minimal.

In order to construct the generalized coordinates of one zone given the discrete transformation defined by another zone, a local geometric variation is assumed in each cell. A bilinear variation in each cell,

$$\vec{r} = \vec{a}_1 + \vec{a}_2\eta + \vec{a}_3\zeta + \vec{a}_4\eta\zeta, \quad (25)$$

leads to a mismatch in the discrete boundary definition between the two grids near a curved boundary, as illustrated in Fig. 2. The boundary mismatch is not generally an issue for meshes encountered in computations for the Euler equations, since the mismatch is a small fraction of the area of the cells adjacent to the boundary. For solutions to the Navier-stokes equations, in which the grids are highly clustered near the boundary to resolve the viscous layers at high Reynolds numbers, the situation depicted in Fig. 2(b) is not uncommon. In Fig. 3(a), the cell centers of one zone are shown in the generalized coordinate frame of the other zone (unit spacing in η and ζ); the two cell centers nearest the boundary actually lie outside the discrete boundary of the other zone. For the zones shown, the grid spacing normal to the boundary is the same for both zones and, in the outer part of the grid, the cell centers lie midway between the grid lines, as expected.

The surface definition can be substantially improved by using a degenerate biquadratic fit in the direction tangential to the boundary, i.e.

$$\vec{r} = \vec{a}_1 + \vec{a}_2\eta + \vec{a}_3\zeta + \vec{a}_4\eta\zeta + \vec{a}_5\eta^2 + \vec{a}_6\eta^2\zeta. \quad (26)$$

This form ensures that the boundaries of the cells are continuous between the zones, if the grid point data is augmented by additional edge points in the η direction. For each cell edge along $\zeta = \text{constant}$, additional points are determined by passing a least squares quadratic curve through the 2 grid points defining a cell edge and the nearest grid point on either side. For the zones in Fig. 2, the grid mismatch is reduced from $O(1)$ to $O(10^{-2})$, as shown in Fig. 3(b), wherein all the cell centers lie very close to midway between the grid points of the other.

The generalized coordinates of each cell center to be interpolated is determined through a nonlinear iterative procedure. A nearest enclosing cell is guessed based on the distance from the grid point data to the cell center and then updated by solving for (η, ζ) from Eq. (26) through a Newton procedure, until the computed (η, ζ) lies within the candidate cell boundary. The conserved variables are then interpolated using the linear fit of Eq. (24).

Computational Results

The grid topologies used are shown in Fig. 4. A 2-zone grid, shown in Fig. 4(a), is described in detail by Ghaffari et. al.¹⁰ The grids were generated in each block using an H-O topology with transfinite interpolation. The two blocks are patched together at the strake apex. The upstream block contains 31 and 65 points in the circumferential and normal directions, respectively, and the downstream block contains 65 points in both directions. The 2-block grid contains a total of 185,000 grid points and a spacing normal to the boundary of $0.8 \times 10^{-4}z$. At the zonal interface, the grid lines are coincident only at the surface and in the longitudinal plane of symmetry and were generated with no requirements for grid alignment in the interior of the grid. The disadvantage of the 2-block grid topology is that the circumferential grid clustering at the strake propagates forward into and ahead of the nose region.

A three-block grid is shown in Fig. 4(b-c). Part of the upstream block in Fig. 4(a) is replaced with an O-O topology. The additional block gives a much better resolution of the forebody geometry; the additional zonal interface is evident on the body surface and in the longitudinal plane of symmetry. A number of different grids were used in the first block. The finest, Fig. 4(b), has 65 and 73 points in the circumferential and normal directions, with a normal spacing of $0.1 \times 10^{-4}z$; the coarsest, Fig. 4(c), has 31 and 49 points in the circumferential and normal directions, with a normal spacing of $0.5 \times 10^{-4}z$.

Laminar Flow Computations

Symmetry plane pressure contours using the spatial-flux and time-flux conservation strategies for the 2-block grid are shown in Fig. 5 for the conditions considered in detail by Ghaffari et. al.¹⁰: $M_\infty = 0.6$, $R_e = 0.8 \times 10^6$, $\alpha = 20$ deg. Both calculations interpolate across the zonal interface using Eqs. (21) and (23). The two solutions are nominally the same; any differences are on the order of the truncation error of the calculations.

Computed total pressure contours and surface particle traces are shown in Fig. 6 at a high angle-of-attack, laminar flow condition: $M_\infty = 0.3$, $R_e = 0.74 \times 10^6$, $\alpha = 30$ deg. The primary and secondary separation lines on the forebody are evident, as well as the secondary separation line on the strake. The vortices shed along these lines are very shallow and lie close to the body surface, especially in comparison to the primary vortex shed from the strake. The primary separation line on the forebody leads into a large region of reverse flow ahead of and predominantly under the strake apex. Under the strake along the body, a primary separation line is evident, leading to a vortex impinging on the strake lower surface. Along the fuselage above the strake, a separation line extending downstream from the apex is evident. The streamlines pass smoothly through the zonal interfaces. The overall flowfield is qualitatively similar to the laminar calculations given by Ghaffari et. al.¹⁰ at $\alpha = 20$ deg.

Oil flows from a test in the Basic Aerodynamics Research Tunnel (BART)¹⁸ at NASA Langley Research Center for the same angle of attack but slightly lower Reynolds number, $R_e = 0.2 \times 10^6$, are compared to the computed particle traces in Fig. 7. The experimental oil flows demonstrate a striking resemblance to the computations.

The effect of grid refinement is shown in Fig. 8 for the 3-block grid at the experimental Reynolds number. The interface interpolations were done with the time-flux approach, using Eq. (26) and the nonconservative interpolations of Eq. (24). With the finer grid, the forebody secondary separation line is straighter, lying nearer to the leeward plane of symmetry, in better agreement with the experiment. The flow over the two downstream blocks is largely the same. Some apparent differences are due to the fact that the seeding positions for the particle traces are not identical for Fig. 8(a) and 8(b). As can be seen by comparing Figs. 7 and 8, under the laminar assumption there is very little effect of Reynolds number over the range considered. In Fig. 8, the particle traces originating in a block are confined to remain in that block; the surface flow, however, passes smoothly through the two zonal interfaces. The first zonal interface has a variation in both the circumfer-

ential and normal spacing of the grid on either side, and the improved interpolation obtained with the bi-quadratic surface fit to the geometry is critical in obtaining the smooth results shown.

Turbulent Flow Computations

Comparisons with wind-tunnel results at higher Reynolds numbers and with in-flight results show markedly different surface oil flow patterns.⁹ The flight-test results correspond to a Reynolds number of 10-15 million based on \bar{z} and show primary and secondary separation lines on the forebody much closer to the leeward plane of symmetry. Computed particle traces at flight Reynolds number for the 3-block grid of Fig. 4(b) are compared with the flight-test results¹⁰ in Fig. 9. The primary and secondary separation lines on the forebody are well predicted. The extent of separation in the strake apex region is considerably reduced and the secondary separation line on the strake is moved outward from the laminar condition, as expected. The computed secondary separation line on the strake does not extend into the forward region of the strake; a reflex in the particle traces is indicated in that region, which generally leads with grid refinement to a clearly defined separation line. In this context, the grid spacing in block 1 corresponds to $y^+ \approx 2$ and is considerably finer in the normal direction than in either of the two downstream blocks.

Concluding Remarks

A patched grid algorithm for complex configurations has been described. The work is an extension to the longitudinally-patched approach of Refs. 2-3, allowing for the analysis of grids which are highly stretched in the normal direction to resolve viscous flows, and for arbitrarily-shaped patch surfaces. Two algorithms, a spatial-flux and a time-flux conservation approach, have been used across zonal interfaces with few differences noted. The latter approach is somewhat more flexible and can be easily extended to handle more complex situations, such as overlapped and embedded grids. A longer term objective of the present domain decomposition approach is for the only constraint on the grid topology to be that the grids span the entire physical domain. The computational algorithm should be general enough to automatically determine the necessary connections between the domains to ensure a globally second-order accurate solution.

Applications using the algorithm have been made to the F-18 forebody-strake configuration at $\alpha = 30$ deg over a range of Reynolds number. The laminar flow calculations agree well with the wind-tunnel results at $R_z = .2 \times 10^6$. The turbulent flow calculations are substantially different in the separation line positions and

agree well with flight-test results at $R_z = 10 \times 10^6$. The wind-tunnel results at $R_z \approx 1 \times 10^6$ exhibit a separation pattern different from either calculation;⁹ the difference is associated with the transition from laminar to turbulent flow. The laminar separation bubble described in Ref. 9 from flow visualisations occurs in the region of the primary separation line predicted by the present algorithm, assuming a laminar viscous model.

Acknowledgments

NASA-Langley Research Center sponsored the work of the 2nd and 3rd authors under NASA Grant (NAG1-866) and that of the 4th author under NASA Contract No. NAS1-17919. The authors wish to thank Mr. Scott Kjølgaard of NASA Langley Research Center for providing the flow visualisations of the F-18 configuration in BART and Mr. Dave Fisher of the NASA Dryden Flight Research Facility for providing surface flow visualization photographs of the NASA F-18 HARV along with supporting flight data.

References

- ¹ Rai, M. M.: A Relaxation Approach to Patched-Grid Calculations with the Euler Equations. AIAA Paper No. 85-0295, 1985.
- ² Walters, R. W.; Reu, T.; McGrory, W. D.; Thomas, J. L.; and Richardson, P. F.: A Longitudinally-Patched Grid Approach with Applications to High Speed Flows. AIAA Paper No. 88-0715, 1988.
- ³ Walters, R. W.; Reu, T.; Thomas, J. L.; and McGrory, W. D.: Zonal Techniques for Flowfield Simulation About Aircraft. ASME Symposium on Advances and Trends in Computational Structural Mechanics and Fluid Dynamics, Washington, D.C., October 1988.
- ⁴ Benek, J. A.; Buning P. G.; and Steger, J. L.: A 3-D Chimera Grid Embedding Technique. AIAA Paper No. 85-1523CP, 1985.
- ⁵ Hessinius, K.A. and Rai, M. M.: Three Dimensional, Conservative, Euler Computations Using Patched Grid Systems and Explicit Methods. AIAA Paper No. 86-1081, 1986.
- ⁶ Kathong, M.; Smith, R.E.; and Tiwari, S.N.: A Conservative Approach for Flow Field Calculations on Multiple Grids. AIAA Paper No. 88-0224, 1988.
- ⁷ Thomas, J.L.; Rudy, D.H.; Chakravarthy, S.R.; and Walters, R.W.: Patched-Grid Computations of High-Speed Inlet Flows. Symposium on Advances and Applications in Computational Fluid Dynamics, Chicago, Illinois, ASME FED Vol. 66, 1988, pp. 11-22.
- ⁸ Walters, R.W.; Thomas, J.L.; and Switzer, G.F.: Aspects and Applications of Patched Grid Calculations. AIAA Paper No. 86-1063, 1986.

⁹ Fisher, D. F.; Richwine, D. M.; and Banks, D. W.: Surface Flow Visualization of Separated Flows on the Forebody of an F-18 Aircraft and Wind-Tunnel Model. NASA TM 100436, 1988.

¹⁰ Ghaffari, F.; Luckring, J. M.; Thomas, J. L.; and Bates, B.L.: Navier-Stokes Solutions About the F/A-18 Forebody-LEX Configuration. AIAA Paper No. 89-0338, 1989.

¹¹ Baldwin, B. S.; and Lomax, H.: Thin Layer Approximation and Algebraic Model for Separated Turbulent Flows. AIAA Paper No. 78-257, 1978.

¹² Degani, D.; and Schiff, L. B.: Computation of Supersonic Viscous Flows Around Pointed Bodies at Large Incidence. AIAA Paper No. 83-0034, 1983.

¹³ Vatsa, V. N.; Thomas, J. L.; and Wedan, B. W.: Navier-Stokes Computations of Prolate Spheroids at Angle of Attack. AIAA Paper No. 87-2627-CP, 1987.

¹⁴ Thomas, J. L.; Taylor, S. L.; and Anderson, W. K.: Navier-Stokes Computations of Vortical Flows Over Low Aspect Ratio Wings. AIAA Paper No. 87-0207, 1987.

¹⁵ Van Leer, B.; Thomas, J. L.; Roe, P. L.; and Newsome, R. W.: A Comparison of Numerical Flux Formulas for the Euler and Navier-Stokes Equations. AIAA Paper No. 87-1104CP, 1987.

¹⁶ Van Leer, B.: Upwind-Difference Methods for Aerodynamic Flows Governed by the Euler equations. Lectures in Applied Mathematics, Vol. 23, Part 2, AMS, Providence, 1985, pp. 327-336.

¹⁷ Ramshaw, J. D.: Conservative Resoning Algorithms for Generalized Two-Dimensional Meshes. Journal of Computational Physics, Vol. 59, 1985, pp. 193-199.

¹⁸ Sellers, W. L. III; and Kjølgaard, S.O.: The Basic Aerodynamics Research Tunnel - A Facility Dedicated to Code Validation. AIAA Paper No. 88-1997CP, 1988.

¹⁹ Fisher, D. F. and Meyer, R.R. Jr : Flow Visualization Techniques for Flight Research. NASA TM 100455, October, 1988.

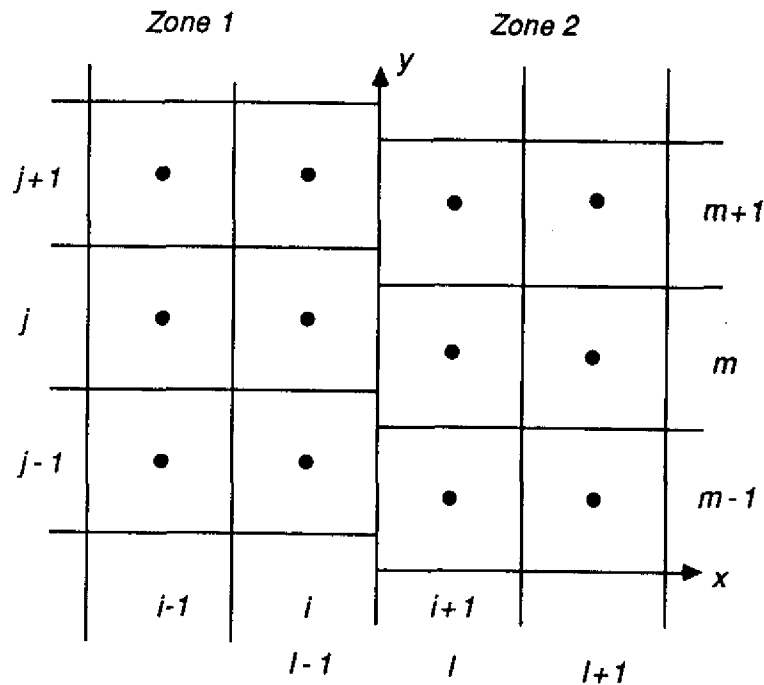
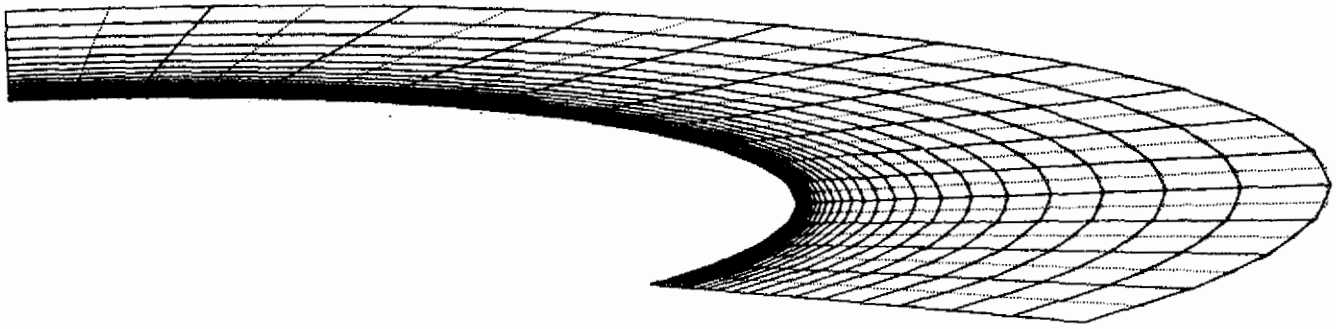
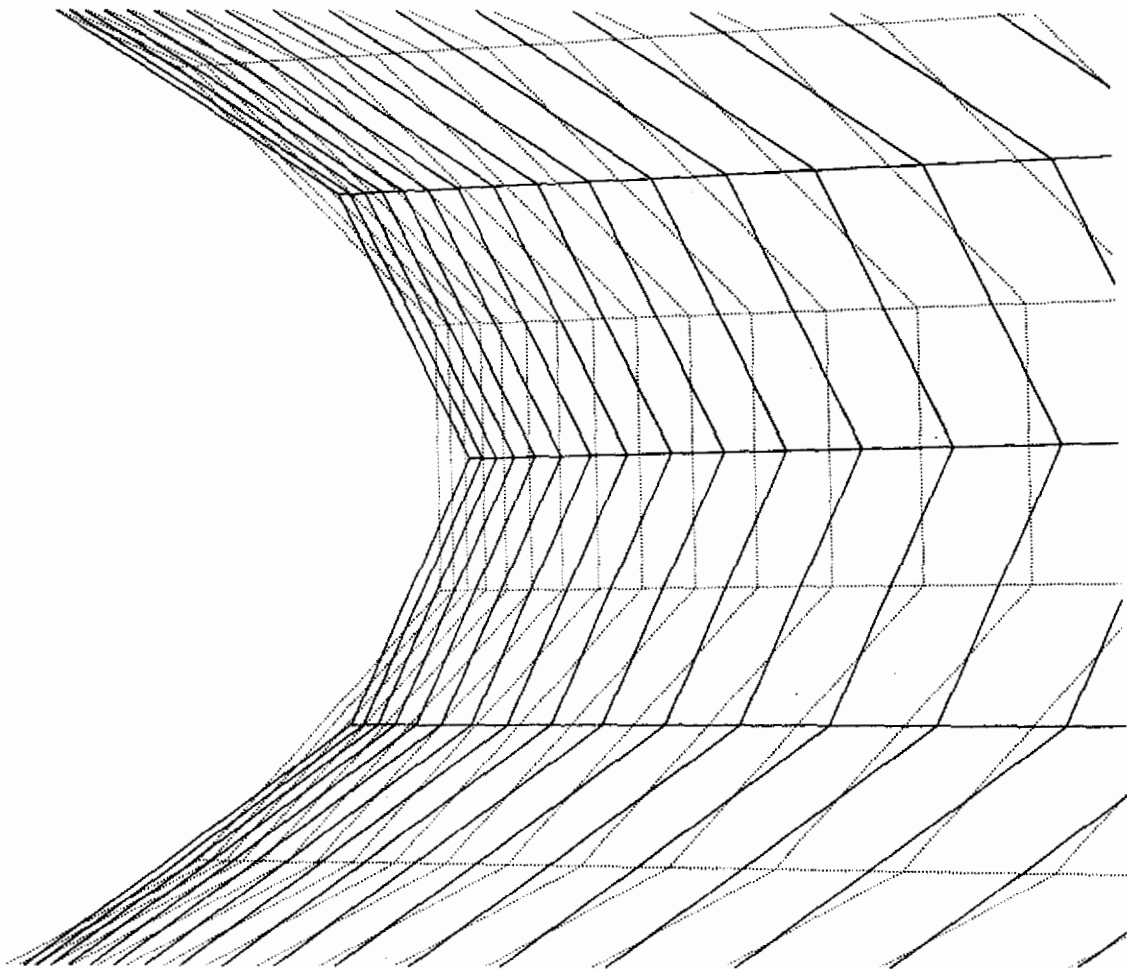


Fig. 1.- Two-dimensional zonal interface.

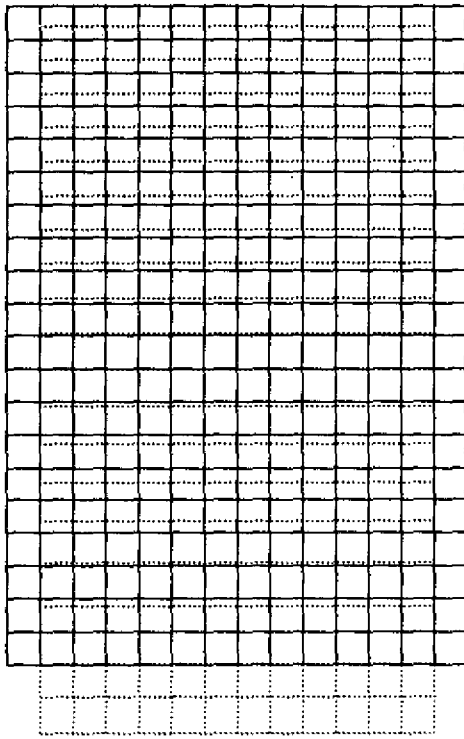


(a) Farfield view.

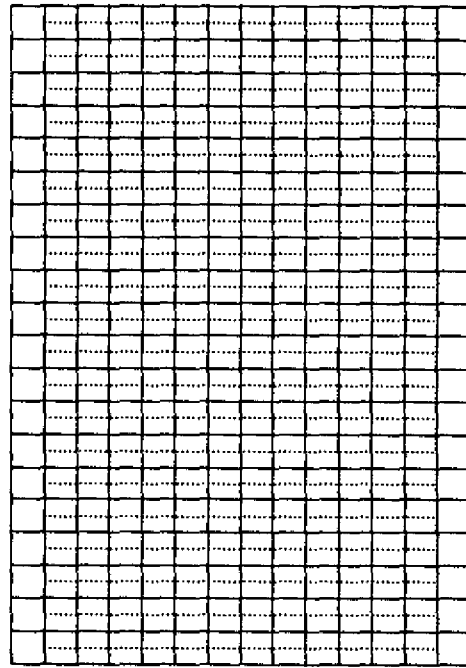


(b) Nearfield view.

Fig 2.- Coincident zonal interface defined by zone 1 grid (solid lines) and zone 2 grid (dotted lines) for partial ellipse section.

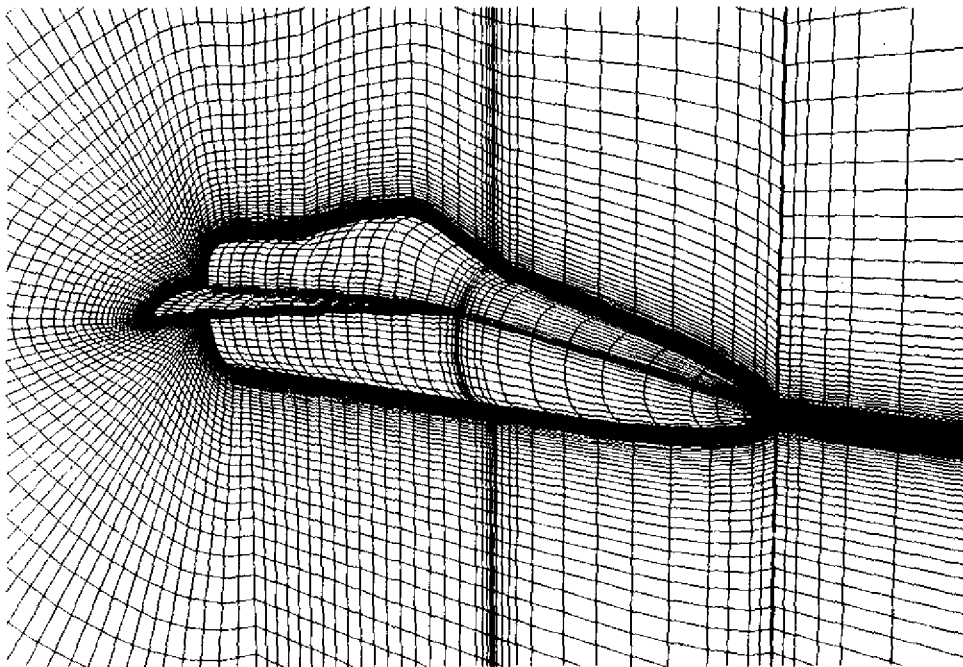


(a) Bilinear basis.



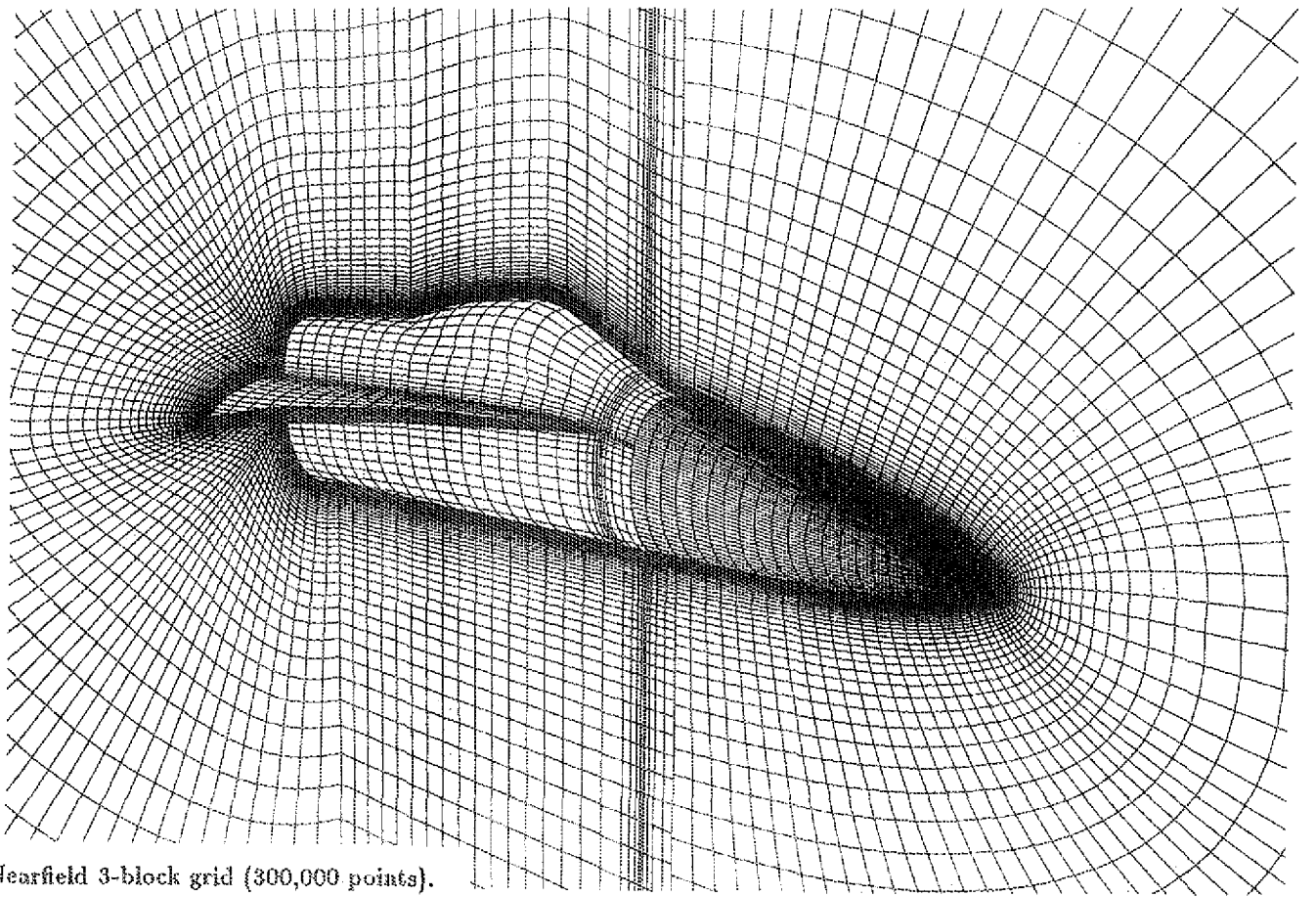
(b) Biquadratic basis.

Fig 3.- Generalized coordinates of zone 2 cell-center locations (dotted lines) in transformation defined by zone 1 grid (solid lines) for partial ellipse section.

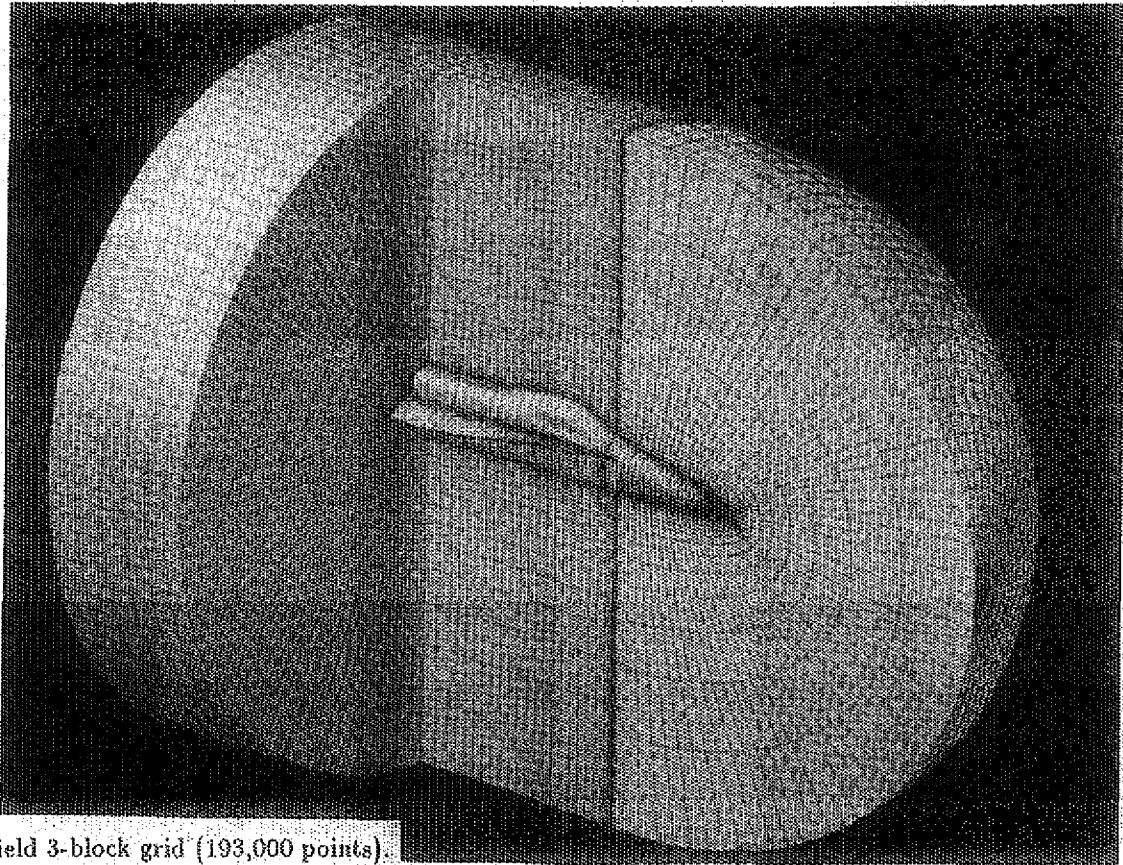


(a) Nearfield 2-block grid (185,000 points).

Fig 4.- F-18 forebody-strake grid.



(b) Nearfield 3-block grid (300,000 points).



(c) Farfield 3-block grid (193,000 points).

Fig 4.- Concluded.

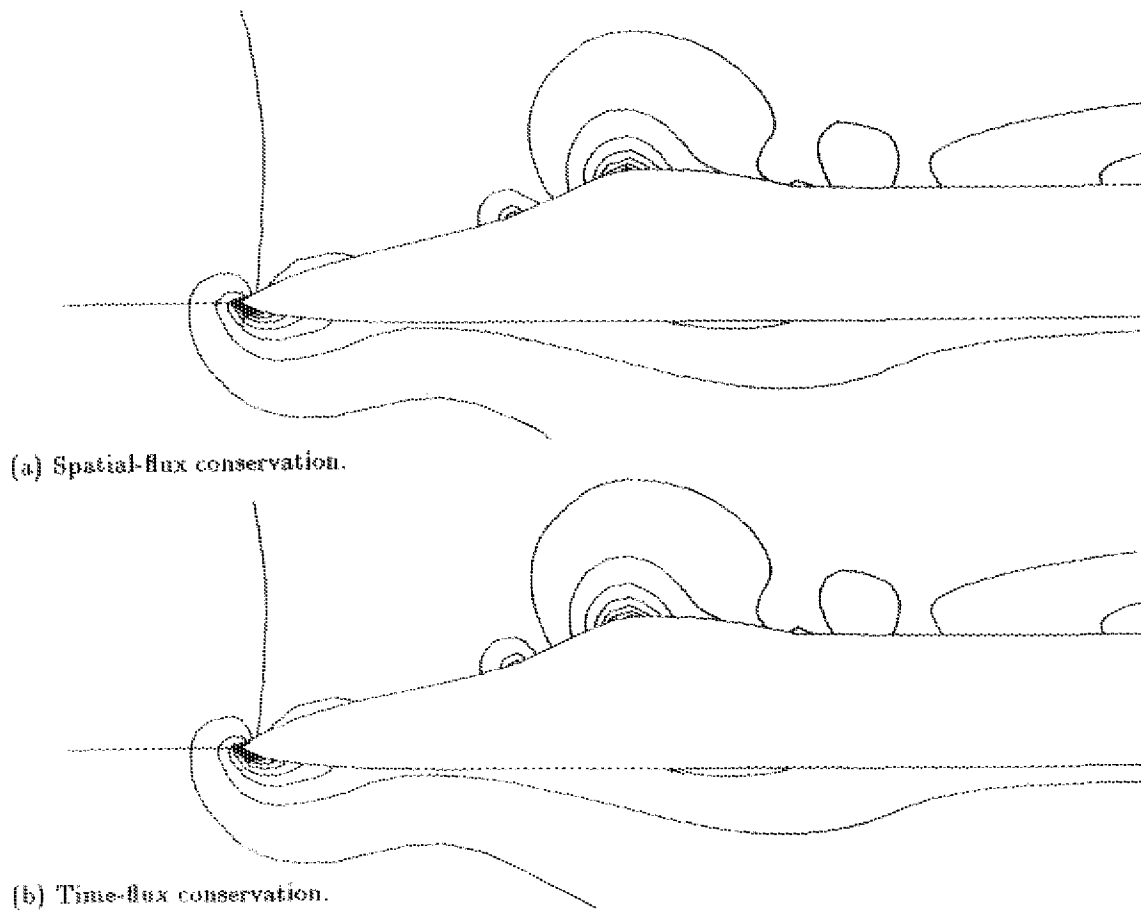


Fig 5.- Centerline pressure contours. $M_\infty = 0.6$, $R_n = 0.8 \times 10^6$, $\alpha = 20$ deg.

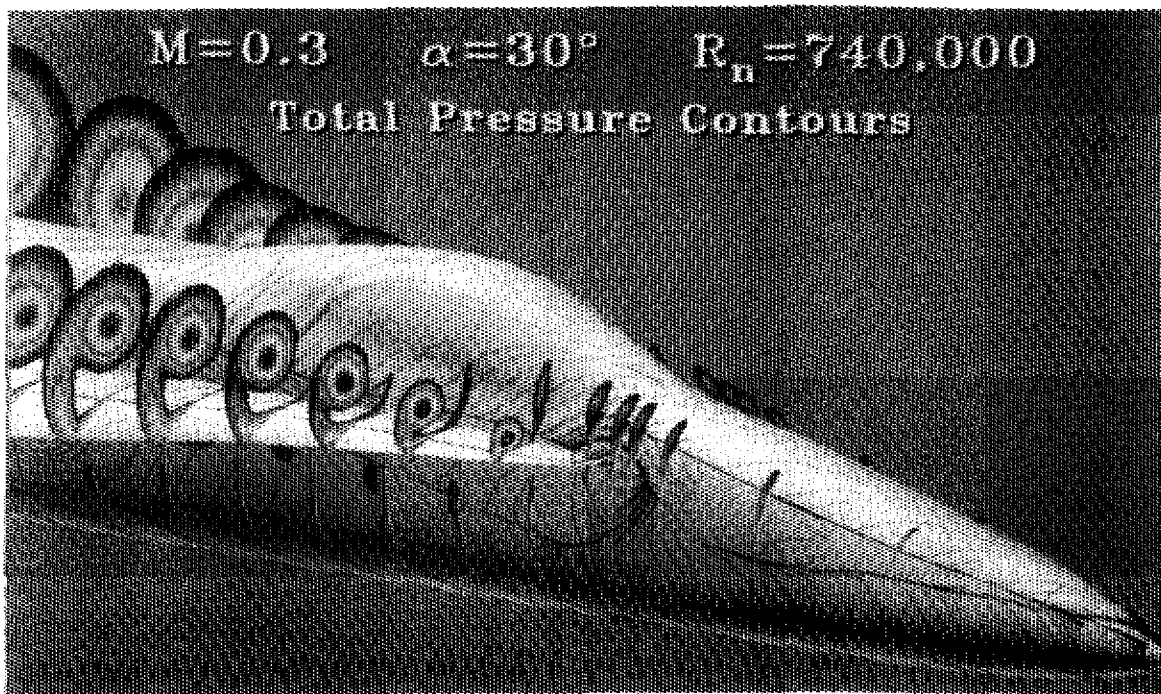
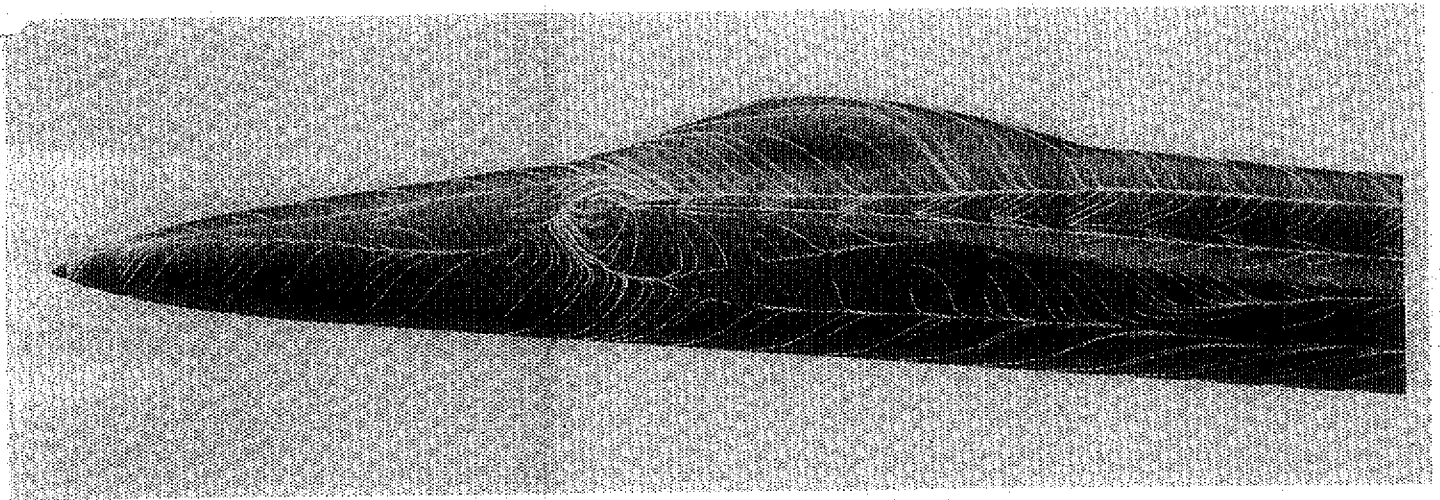
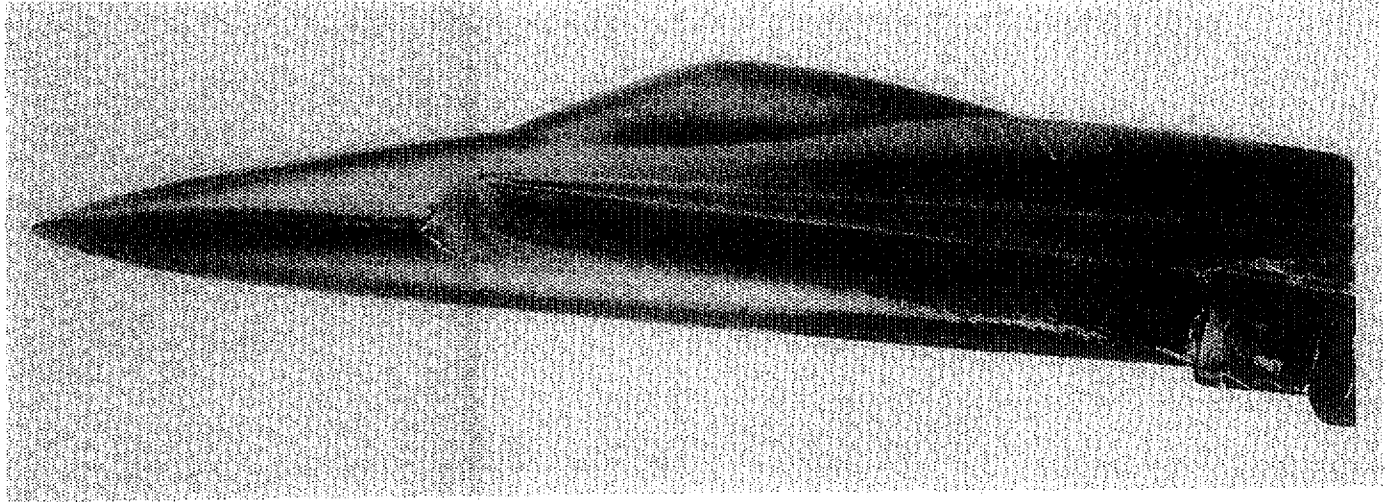
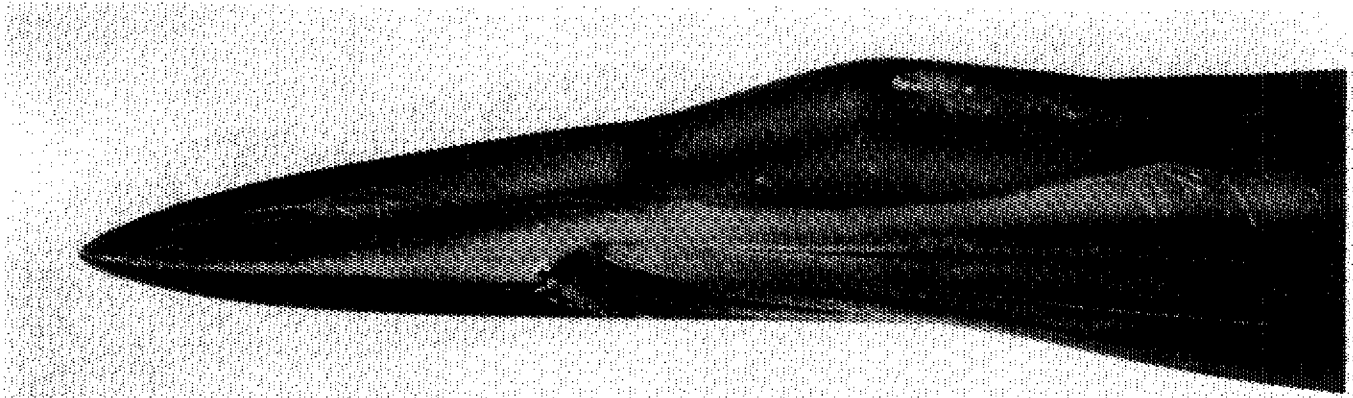


Fig 6.- Total pressure contours and surface particle traces for forebody-strake using 2-block grid. $M_\infty = 0.3$, $R_n = 0.74 \times 10^6$, $\alpha = 30$ deg.



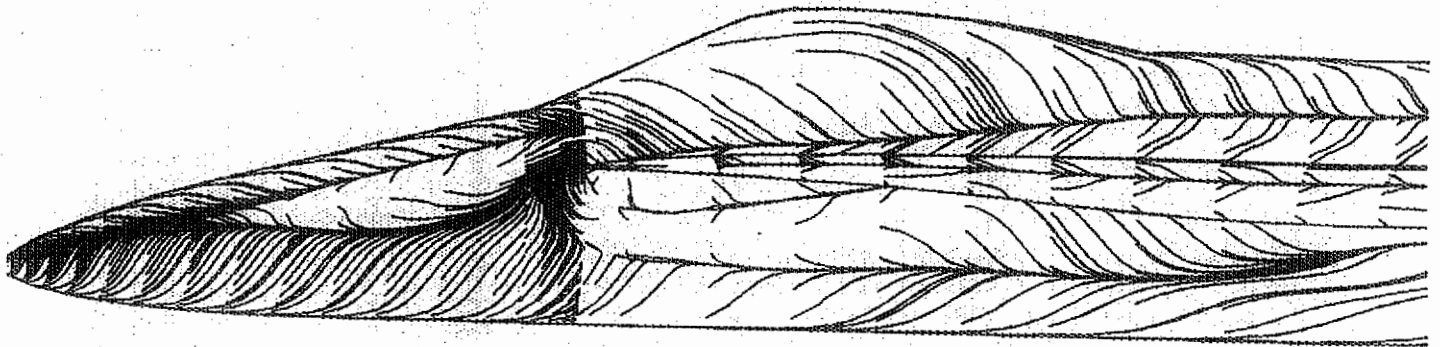
(a) Side view.

Fig 7.- Wind-tunnel (top) and computed (bottom) surface flow patterns on forebody-strake at low-speed, laminar flow conditions. $\alpha = 30$ deg.

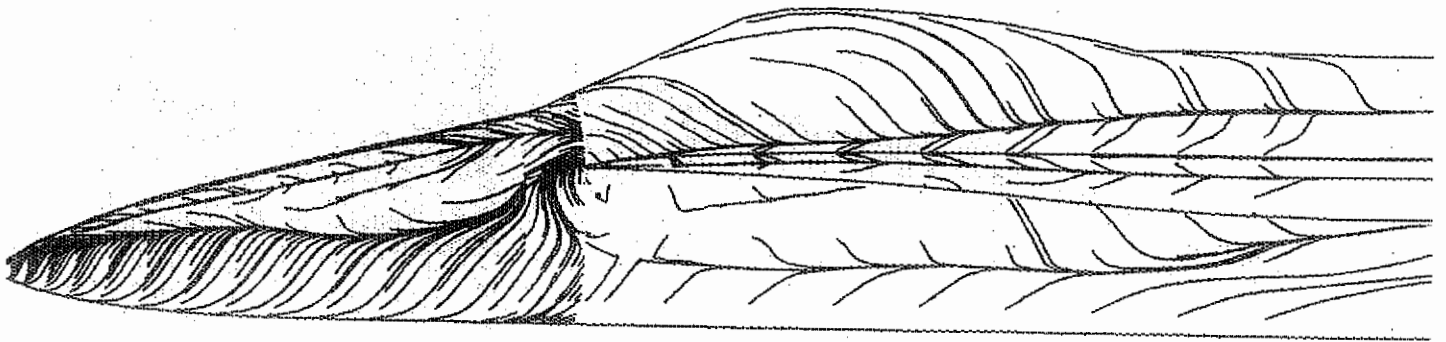


(b) Three-quarter side view.

Fig 7.- Concluded.

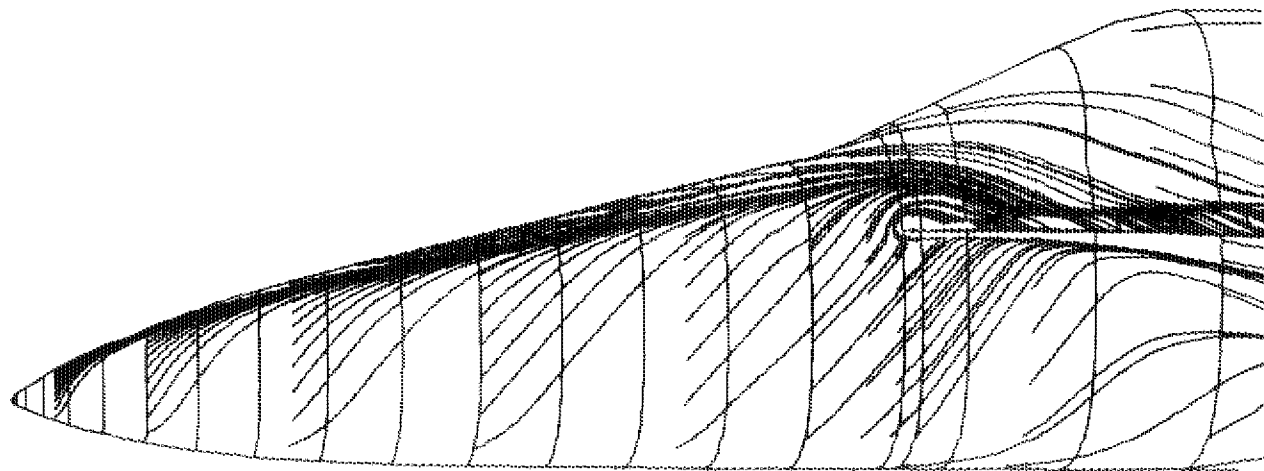
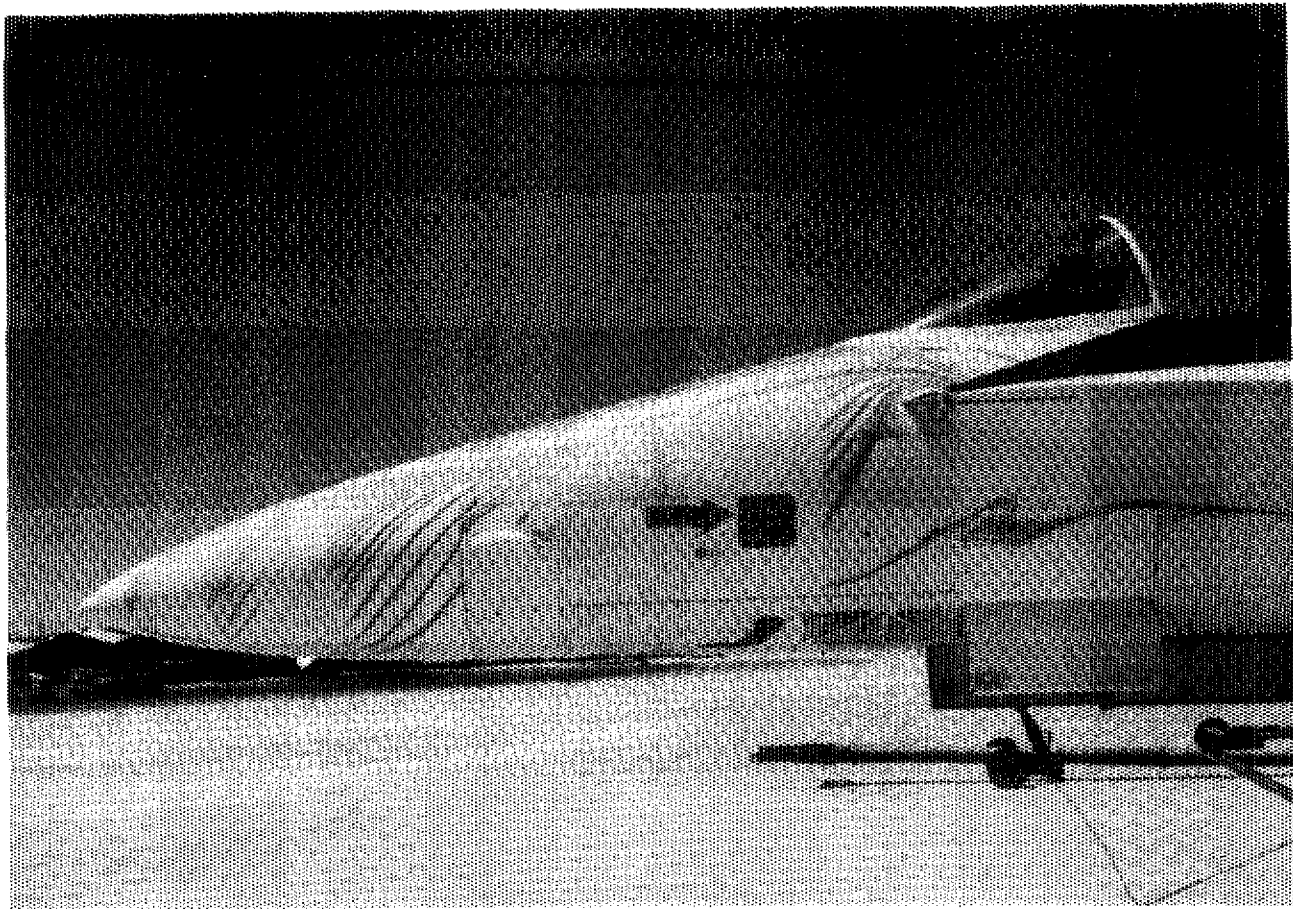


(a) 3-block grid (193,000 grid points).



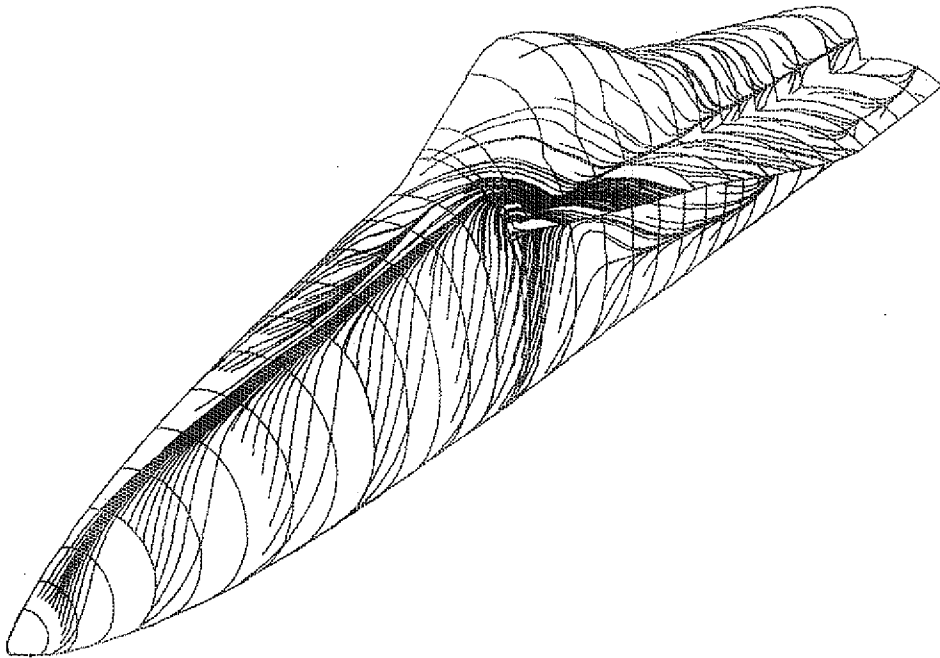
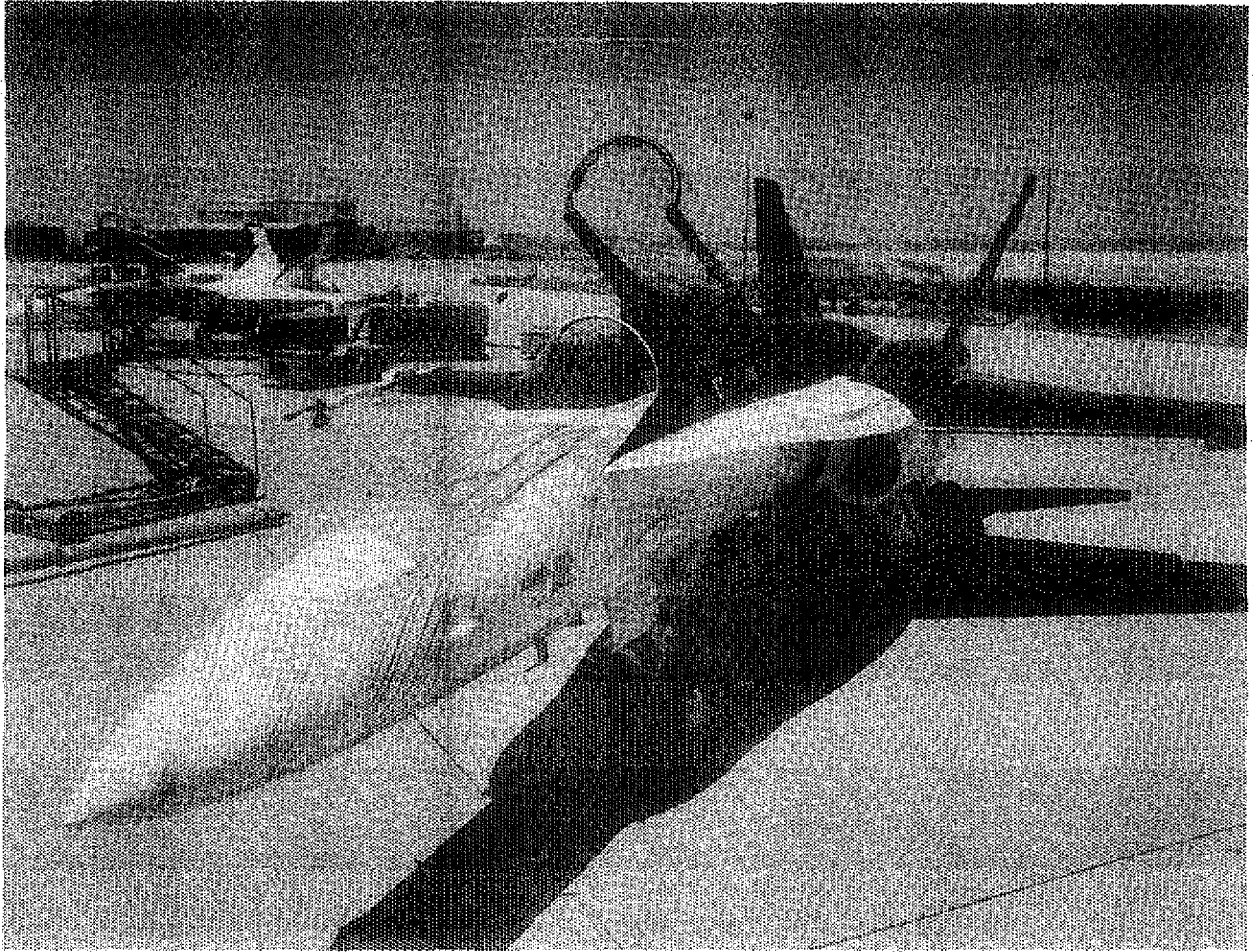
(a) 3-block grid (282,000 grid points).

Fig 8.- Effect of grid refinement on forebody-strake configuration. Side view, $M_\infty = 0.3$, $R_e = 0.2 \times 10^6$, $\alpha = 30$ deg.



(a) Side view.

Fig 9.- Flight-test (top) and computed (bottom) surface flows for F-18 configuration. $M_\infty \approx 0.3$, $Re \approx 10 \times 10^6$, $\alpha = 30$ deg.



(b) Three-quarter front view.

Fig 9.- Concluded.